Progress in Additive Manufacturing (2023) 8:1641–1651
https://doi.org/10.1007/s40964-023-00431-w

FULL RESEARCH ARTICLE

Effects of powder properties on the 3D printing of $BaTiO_3$ ceramic resins by stereolithography

Elena Stefan[1] · Terje Didriksen[1] · Tor Olav Sunde[1] · Marie-Laure Fontaine[1] · Henrik Ræder[1] · Per Martin Rørvik[1]

Received: 28 September 2022 / Accepted: 11 March 2023 / Published online: 23 March 2023

Abstract
Stereolithography is a layer-by-layer building fabrication technique enabling production of advanced ceramic 3D shapes that are not achievable by other methods. Critical parameters of stereolithography are associated with the preparation of a ceramic resin exhibiting suitable rheological and optical properties, as well as tunable curing property to achieve the desired level of resolution of complex 3D parts. However, tailoring the cure depth for each layer is challenging for functional ceramics due to their high refractive index giving increased light scattering. Here, the stereolithography 3D printing of $BaTiO_3$ ceramic resins is investigated by employing a desktop 3D printer ($\lambda = 405$ nm) and a commercial base resin. The effects of two $BaTiO_3$ powders with different size distributions (one micro-sized powder with grains in the range 1–20 µm, and one agglomerated nano-sized powder in the range 60–100 nm), on the viscosity and curing characteristics of the ceramic resins were investigated. It is shown that the nano-sized powder resulted in increased viscosity, increased scattering, and reduced cure depth compared to the micro-sized $BaTiO_3$ ceramic resin. In general, the cure depth decreased with increasing ceramic loading. Successful prints were obtained for an overcuring of at least 40% between layers to assure good adherence between the layers. The printing properties of the ceramic resins from both powders were suitable for printing green parts with 50 µm layer thickness.

Keywords Barium titanate · Particle size · Viscosity · Polymerization · Stereolithography

1 Introduction

Advances in ceramic additive manufacturing can give significantly improved performance of functional ceramic devices due to novel shape designs that cannot be obtained by traditional shaping methods such as injection molding, vacuum casting, slip casting, etc. [1, 2]. Stereolithography (SLA) has several advantages for additive manufacturing of ceramics, such as high resolution for printing complex parts with smooth surface finish and few printing defects. Printing of solid parts is achieved by exposing a photosensitive resin with ceramic particles to a light source to initiate a photopolymerization reaction which solidifies the polymer in a layer-by-layer building process [1, 3]. The polymer is removed by subsequent thermal treatment to obtain the final ceramic part.

Successful fabrication of ceramics by stereolithography is defined by obtaining the desired shape with acceptable geometrical tolerances, obtaining a feasible product size and wall thickness, avoiding formation of cracks, and achieving high density of the final ceramic parts. The success rate relies on the properties of the ceramic resin, with ideally low viscosity, appropriate curing characteristics, and high ceramic loading, for obtaining dense and defect-free ceramics [4, 5]. The inclusion of ceramic particles in the resin changes the apparent characteristics of the photocurable resin, and stereolithography of ceramic resins is therefore more challenging than conventional base resins for printing polymers [6].

The ceramic particles generate significant scattering upon illumination, which is determined by the difference in refractive index between the base resin and the ceramic material [7, 8]. The scattering effect results in the deviation of light from the normal direction to the printing surface, giving

✉ Per Martin Rørvik
per.martin.rorvik@sintef.no

[1] SINTEF, Oslo, Norway

polymerization in undesired directions. The effect of the refractive index contrast between a ceramic and a photocurable resin was evaluated by Gentry and Halloran [3, 7, 8]. They measured the broadening of the cured lines of a base resin and of resins mixed with structural ceramic particles (alumina, silica, mullite, and zircon) exhibiting low and high refractive index contrast. The cured line of a base resin is sharp, with excellent lateral resolution of the print, while the ceramic resins have a broadening of the cured line. This effect becomes more significant for large differences in the refractive index between the ceramic and the base resin and it results in loss of details and dimensional accuracy in the x-y plane [3, 7, 8]. In accordance with these authors, Bae [4] discusses the effect of the refractive index contrast, particle size and ceramic loading on the printability of a ceramic resin. For a ceramic material with refractive index ≥2.1 and considering the refractive index of a commercial base resin of typically ~1.5, the sensitivity of the ceramic resin is strongly dependent on the refractive index of the base resin, while for a smaller refractive index contrast, the particle size and the ceramic loading will dominate the resin sensitivity. Figure 1 illustrates the relation between the bandgap and the refractive index for selected ceramics. In general, the refractive index decreases as the band gap increases [9]. As shown in Fig. 1, piezoelectric ceramics such as $BaTiO_3$ and $PbZr_{1-x}Ti_xO_3$ (PZT) have much higher refractive index than commercially available resins for stereolithography, causing challenges for SLA printing.

In addition to light scattering resulting in broadening, light extinction occurs in ceramic resins as a cumulated effect of absorption of light by the ceramic particles, determined by the bandgap and illumination wavelength, and the backward scattering induced by the refractive index contrast between the base resin and the ceramic particles. The light extinction reduces the cure depth in the ceramic resins and the resolution is limited by scattering. The cure depth has great importance, as it should be sufficiently large both to provide adequate interlayer combination of green parts and to fabricate a green part within reasonable time [1, 11].

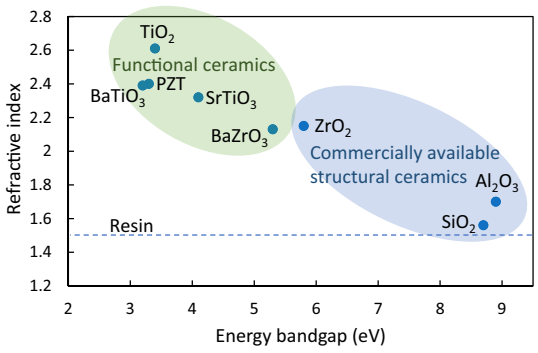

Fig. 1 Relation between bandgap and refractive index for various ceramics [1, 10]. The dashed line represents the typical refractive index for a commercial resin

The rheological behavior of the ceramic resin also affects the success of the printing process, as the ceramic resin must be stable to avoid sedimentation during the printing process, and ideally it must have the ability of self-levelling. A typical recommended upper limit of the viscosity is 3 Pa·s at 10 s^{-1} shear rate to have processable ceramic resin for SLA [1, 4]. The optimization of the particle size distribution has significant importance for maintaining low viscosity with high ceramic loading, as well as for adjusting the curing characteristics of ceramic resins [12]. Tailoring the viscosity of the resin can also be achieved by additions of dispersants.

Finally, there are also variations of printing results depending on the printer and its functionalities. In general, very few studies of SLA of functional ceramics make use of desktop printers. This can be imparted to the more complex functionalities available in advanced printers, such as in-built facility for levelling of the resin upon the layer-by-layer building process, the use of top-down building process, possibility for mixing the resin avoiding sedimentation and/or thixotropy effect, etc.; however, such printers are much more expensive than desktop printers.

The current work assesses the effects of the particle size and distribution of a high refractive index oxide material ($BaTiO_3$) on the rheology and the photocuring properties of ceramic resins prepared with a ceramic loading of $BaTiO_3$ powder ≤ 50 wt%. The printability of $BaTiO_3$ green parts is assessed by evaluating the geometric resolution of the printed parts using a desktop stereolithography 3D printer. Insights on the effect of overcuring to achieve better interlayer adhesion are also presented.

2 Materials and methods

$BaTiO_3$ powders were purchased from Nanografi Nano Teknoloji, Turkey, and are referenced as $BaTiO_3$ micro-powder (BTO1) and nano-powder (BTO2). The powders were mixed with dispersant Triton X-100 (1 wt%) and isopropanol (solvent/ceramic powder ratio 44/56 wt%) in a 250 mL ZrO_2 milling container with ZrO_2 balls (diameter 10 mm, in total 17.6 mL, ball/ceramic powder ratio 57/43 wt%) using a planetary miller operated for 2 h at 210 rpm. After milling, the powders were dried at 80 °C for 16 h. Ceramic resins were prepared by mixing the powder/dispersant mixtures with an acrylate-based photosensitive commercial resin (Genesis development resin, Tethon 3D, USA) with 2,4,6-trimethylbenzoyldiphenylphosphine oxide (2–4%) as photoinitiator in a planetary miller for 2 h at 210 rpm. The resulting composite resins were prepared with the following ceramic loadings: for BTO1: 20, 28.5, 40, 45 and 50 wt%; and for BTO2: 33, 40 and 50 wt%.

To investigate the effect of not breaking up the BTO2 agglomerates on the properties of the ceramic resin, the BTO2 nano-powder was calcined at 930 °C for 1 h to coarsen the powder, and subsequently placed in a beaker filled with ethanol for 10 min to allow sedimentation and separation of large particles/agglomerates. The supernatant was removed, and the settled powder was dried at 80 °C for 16 h. Approximately 50 wt% of the calcined powder was removed by this separation step. The remaining powder is onwards named BTO2-set. The BTO2-set powder was mixed with Triton X-100 (1 wt%) in isopropanol using a magnetic stirring hot plate. The powder was then dried in air.

The oxide powders were characterized in terms of phase analysis, morphology, UV-Vis absorption, and particle size distribution. X-ray diffraction (XRD) was used for phase identification. The diffractograms were collected on a Panalytical Empyrean with a PIXcel^{3D} hybrid detector, in reflection mode with Cu Kα (Kα1, Kα2) radiation source operated at 36 kV and 36 mA, in a range of 15-80°, with a step size of 0.026° and with 2 s/step, and analyzed with DIFFRAC.EVA software (Bruker) coupled with Crystallography Open Database. The morphology of the powders was analyzed by scanning electron microscopy (SEM) using a FEI NovaNano SEM 650 field emission gun scanning electron microscope. Images were collected in backscattering mode. UV-Vis absorption spectrometry (Agilent Cary 5000) was used to determine the absorption spectra of the oxide powders in the wavelength range of 250–800 nm with 1 nm data interval. Particle size analysis of the powders before and after mixing with dispersant was conducted using laser diffraction with a Malvern Mastersizer 2000. The powders were dispersed in isopropanol by ultrasonication for 5 min in an ultrasonic bath and transferred to the particle size analyzer.

The density of the base resin and the prepared ceramic resins was determined with a TOC VF2098-451 pycnometer. The flow curves for all the prepared resins were established by measuring the viscosity with a rotational viscometer (Dv2t, Brookfield) with shear rates in a range of 2–27 s^{-1}. The flow curves were fitted with the expression for a power law fluid:

$$\eta_{\text{effective}} = Ky^{n-1}, \tag{1}$$

where $\eta_{\text{effective}}$ is the effective viscosity, K is a consistency index, y is shear rate and n gives information about the resin flow behaviour [13, 14]. Resins with $n = 1$ have Newtonian behavior, while resins with $n > 1$ and $n < 1$ have shear thickening and shear thinning behavior, respectively.

A Formlabs Form 1+ stereolithography desktop 3D printer with laser wavelength 405 nm, a printing resolution of 25–100 µm and with options for customization of printing parameters was used to study the curing behavior of the resins, following the Jacob's version of the Beer–Lambert law of absorption [1, 3]:

$$C_{\text{d}} = D_{\text{p}} ln\left(\frac{E}{E_{\text{c}}}\right), \tag{2}$$

where C_{d} is the cure depth, D_{p} is the sensitivity, defined as the depth at which the light intensity is reduced to $1/e$ (36.8%) of its value at the surface, E is the applied energy dose, and E_{c} is the critical energy which is defined as the energy dose that suffices to bring the resin to the gel point. C_{d} values were obtained by exposing the resin to a range of applied energy doses and afterwards measuring the cured thicknesses with a caliper. The plot of measured C_{d} (µm) versus ln(E) (J/cm^2) was used to extract D_{p} and E_{c} as the slope and intercept with the x axis, respectively [3, 15]. All printed parts in this study were cleaned in isopropanol post-printing to remove the excess or unpolymerized resin.

3 Results and discussion

3.1 Structural characterization of the powders

X-ray diffractograms of the $BaTiO_3$ powders show single-phase perovskite phase (Fig. 2). The BTO1 powder has a tetragonal phase identified from the splitting of reflections, for instance seen for (002) and (200) at ~45°. For the BTO2 powder this splitting cannot be seen, indicating a more cubic structure. This is in accordance with other studies reporting

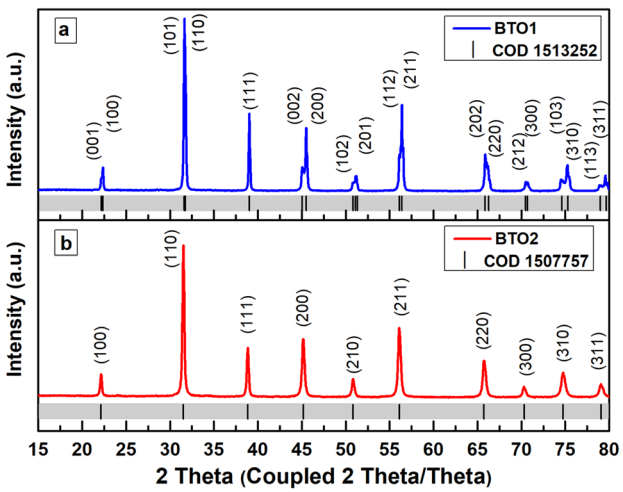

Fig. 2 X-ray diffractograms of the as-received ceramic powders: **a** BTO1 and **b** BTO2. Reference reflections from Crystallography Open Database (COD) are included: 1513252 refers to tetragonal $BaTiO_3$ and 1507757 to cubic $BaTiO_3$

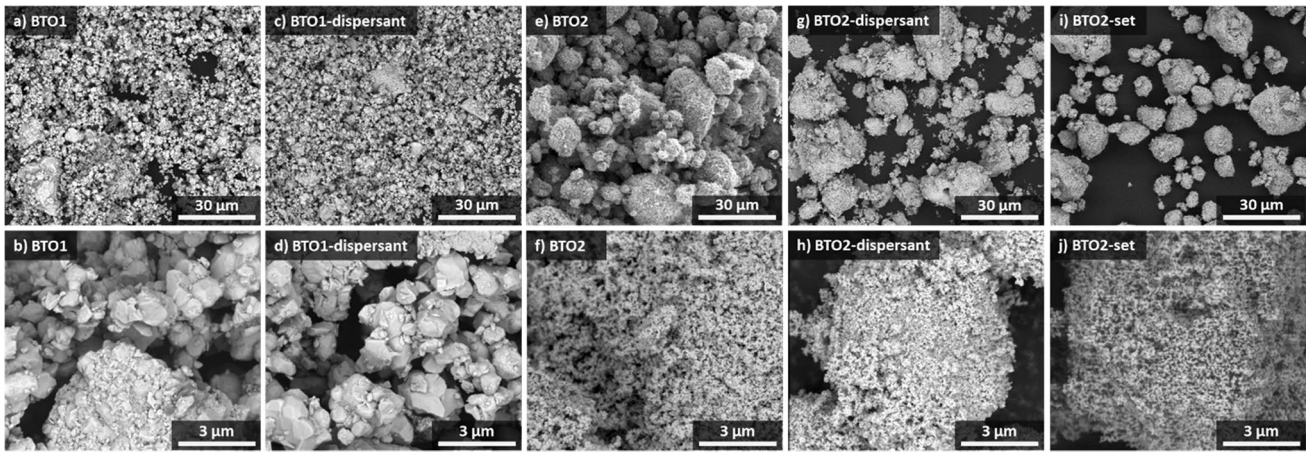

Fig. 3 Micrographs of the ceramic powders before and after mixing with dispersant: **a**, **b** BTO1 as-received, **c**, **d** BTO1 after mixing with dispersant, **e**, **f** BTO2 as-received, **g**, **h** BTO2 after mixing with dispersant, and **i**, **j** BTO2-set

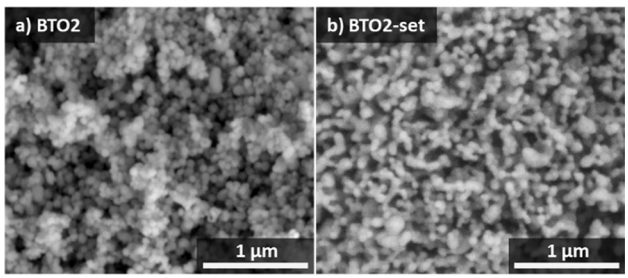

Fig. 4 High-magnification micrographs of BTO2 powders before mixing with dispersant: **a** BTO2 and **b** BTO2-set

that nanosized powder has a *c*/*a* ratio decreasing towards unity [16].

3.2 Microstructural characterization of the powders

The microstructure of the powders is shown in Figs. 3 and 4. Images are presented in backscattering mode. BTO1 powder micrographs show highly compact agglomerates, in the range of 20–30 µm size, as well as smaller grains ranging from 1 to 3 µm size (Fig. 3a, b). Smaller particles of less than 200 nm, possibly generated by crushing the grains/agglomerates during production, can also be seen (Fig. 3b). The microstructure of the BTO1 powder was not significantly changed after ball milling with dispersant (Fig. 3c, d).

The BTO2 powder has a different appearance with round-shaped agglomerates of variable sizes ranging from 1 to 30 µm (Fig. 3e). At higher magnification, it is noticeable that the porous agglomerates consist of nanoparticles, in the range of 60–100 nm size (Figs. 3f and 4a). After ball milling with dispersant, the BTO2 powder had slightly more loose submicron particles and a fraction of broken agglomerates in the range of 1–5 µm (Fig. 3g, h).

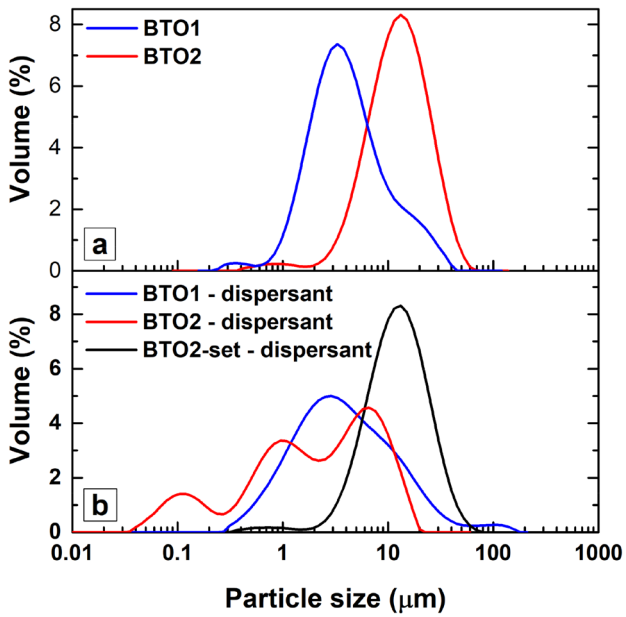

Fig. 5 Particle size distributions of the ceramic powders: **a** before mixing with dispersant, and **b** after mixing with dispersant

The BTO2-set powder has a very similar microstructure to BTO2, even after being thermally treated at 930 °C for 1 h (Fig. 3i, j). At higher magnification, one may observe more pronounced necking between the particles and a coarser microstructure with a higher intergranular porosity of the BTO2-set powder (Fig. 4b) compared to the BTO2 powder (Fig. 4a), caused by the thermal treatment.

Particle size analysis was conducted on the powders before and after mixing with the dispersant. The as-received BTO1 powder has a multimodal size distribution with the main fraction centered on 3 µm, a smaller percentage (~13 vol%) in the range of 10–30 µm, and approximately

3 vol% of particles around 500 nm, as illustrated in Fig. 5a. This distribution is in good accordance with the SEM observations (Fig. 3a, b). Use of a dispersant and ball milling did not change the position of the main fraction, still being centered on 3 µm, but increased the submicron fraction and the fraction of agglomerates of 10–40 µm (Fig. 5b). A small fraction of agglomerates of 40–100 µm size was also observed (2.4 vol%).

The as-received BTO2 powder has a mono-modal size distribution of agglomerates centered around 15 µm size, with a small fraction of ~1.5 vol% of sub-micron agglomerates (Fig. 5a). This correlates well with the agglomerates observed by SEM (Fig. 3e), but the primary nanoparticles inside the agglomerates, clearly seen in Figs. 3f and 4a, are not distinguished in the particle size distribution. After mixing with dispersant and ball milling, the size distribution turned tri-modal with three fractions defined as 0.04–0.3 µm (14.4 vol%), 0.33–3 µm (39.2 vol%) and 3–20 µm (46.4 vol%) (Fig. 5b). Combined with SEM observations (Fig. 3g, h and 4a), the BTO2 powder with dispersant consisted of smaller porous agglomerates containing nano-sized grains, indicating efficient breakage of agglomerates.

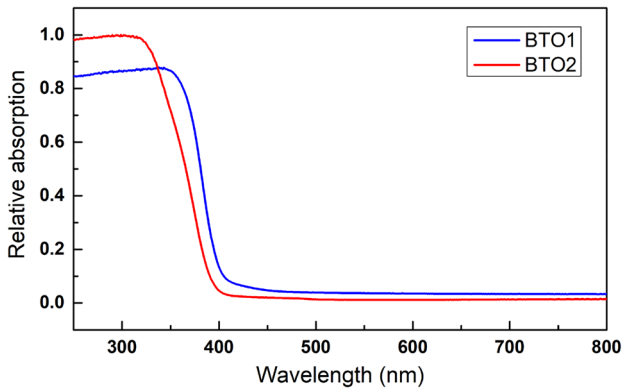

Fig. 6 UV–Vis absorption spectra of $BaTiO_3$ micro-powder (BTO1) and $BaTiO_3$ nano-powder (BTO2)

After the settling procedure and mixing with dispersant, the BTO2-set powder (Fig. 5b) exhibits a Gaussian type of distribution of agglomerate size centered around 15 µm, which is almost identical to the as-received BTO2 powder. Since the dispersant was added without ball milling, the agglomerates were not broken for this powder. The volume fraction of the sub-micron agglomerates for BTO2-set-dispersant was ~1.2 vol%, which was slightly less than for BTO2 (~1.5 vol%), confirming that a fraction of the smallest particles was removed by the settling procedure.

3.3 UV-Vis absorption of powders

The bandgap of $BaTiO_3$ is 3.2 eV and indicates the wavelength at which the oxide absorbs light (387 nm) [17]. The measured absorption for BTO1 and BTO2 powders is shown in Fig. 6. The powders absorb light at slightly different wavelengths: the 50% absorption for the BTO1 powder is at ~381 nm, in a good agreement with the expected value of 387 nm, while for the BTO2 powder it is at ~366 nm. This shift in absorption wavelength is consistent with the difference in particle size of the two powders, as the nanoparticles of BTO2 shift the light absorption to shorter wavelength [18]. As both BTO powders mainly absorb at a shorter wavelength (higher energy) than the laser wavelength used for printing (405 nm), the absorption of light during printing may not hinder the curing of the resins [19, 20].

3.4 Resin density

Table 1 summarizes the density of the ceramic resins measured experimentally and calculated based on the rule of mixtures of two phases (resin + ceramic powder), using the theoretical density of $BaTiO_3$ extracted from XRD refinement (6.028 g/cm^3). As shown in Table 1, there is a good agreement between the experimental data and the ones calculated from the rule of mixture for the three powders used in this study. It can also be seen in Fig. 7, that the density of

Table 1 Ceramic loading of the resins, and densities of the resins as measured experimentally and calculated from the rule of mixtures as function of the ceramic loading

Resin	Ceramic loading (wt%)	Ceramic loading (vol%)	Measured density (g/mL)	Calculated resin density (g/mL)
Base resin (Genesis)	0.0	0.0	1.11	1.11
BTO1-20 wt%	20.0	4.4	1.32	1.33
BTO1-28.5 wt%	28.5	6.8	1.44	1.45
BTO1-40 wt%	40.1	11.0	1.66	1.65
BTO1-45 wt%	44.7	13.0	1.72	1.75
BTO1-50 wt%	50.0	15.6	1.84	1.87
BTO2-33 wt%	32.8	8.2	1.53	1.52
BTO2-40 wt%	40.1	11.0	1.63	1.65
BTO2-50 wt%	50.0	15.6	1.83	1.87
BTO2-set-33 wt%	33.4	8.5	1.52	1.53

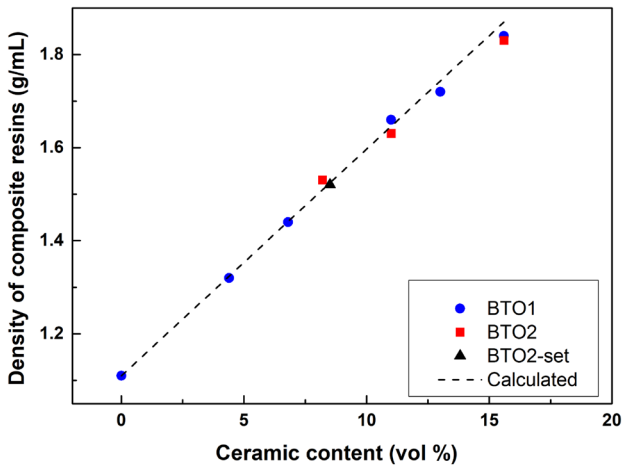

Fig. 7 Evolution of the density of the resins as function of the ceramic loading for the various powders

the composite resins is not affected using different powders in our experimental conditions. The density increases linearly with increasing ceramic loading. There is no evident effect of the particle size or particle size distribution on the density of the ceramic resins, indicating that the base resin infiltrates into the ceramic agglomerates.

3.5 Viscosity

The flow curves for the prepared resins are shown in Fig. 8 and the corresponding power law parameter n is listed in Table 2. For all the resins prepared in this work, the viscosity increases with the ceramic loading, and there is a noticeably higher viscosity of BTO2 resins, ranging from 1480 to 2250 mPa·s, versus BTO1 resins, ranging from 330 to 1150 mPa·s. The BTO2-50 wt% resin had too high viscosity to be measured. It can also be noticed that the viscosity of

Table 2 Power law parameter n for BTO1 and BTO2 ceramic resins

Resin	n
BTO1-20 wt%	1.08
BTO1-28.5 wt%	0.97
BTO1-40 wt%	0.98
BTO1-45 wt%	1.06
BTO1-50 wt%	0.86
BTO2-33 wt%	0.95
BTO2-40 wt%	0.98
BTO2-50 wt%	Out of range
BTO2-set-33 wt%	0.76

the resins prepared with a ceramic loading up to 45 wt% does not evolve as function of the shear rate. This is characteristic of a dominating Newtonian behavior and is confirmed with n ranging from 0.95 to 1.08 for these resins ($n \approx 1$). The BTO1-50 wt% and BTO2-set-33 wt% resins present a shear thinning behavior, in accordance with the lower n factor of 0.86 and 0.76, respectively. Resins with both behaviors are suitable for SLA as the maximum measured viscosity did not exceed 3 Pa·s at 10 s^{-1} and the resins were processable by SLA, as described below.

These data were compared with the effective viscosity of a dilute suspension of rigid non-interacting spherical particles, as defined by Einstein [14]:

$$\eta_{\text{effective}} = \eta_0(1 + 2.5\phi), \tag{3}$$

With η_0 being the viscosity of the base resin, and ϕ the volume fraction of BTO powder, determined using the theoretical density of $BaTiO_3$. As shown in Table 3 and Fig. 9, BTO1 resins with ceramic loadings varying from 20 to 45 wt%, corresponding to a volume fraction ranging from 4.4 to 11.0 vol%, have a calculated effective viscosity in

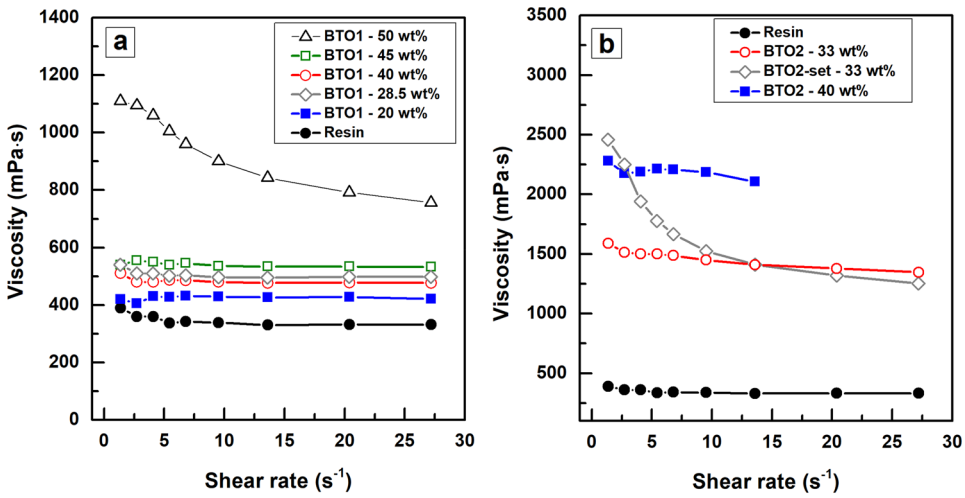

Fig. 8 Viscosity versus shear rate of ceramic resins of **a** BTO1 and **b** BTO2

Table 3 Calculated and measured viscosities for BTO1 and BTO2 ceramic resins

Resin	η calculated (Pa·s)	η measured at 9.5 s^{-1} (Pa·s)
Base resin (Genesis) (n_o)	–	0.33
BTO1-20 wt%	0.37	0.43
BTO1-28.5 wt%	0.39	0.50
BTO1-40 wt%	0.42	0.48
BTO1-45 wt%	0.44	0.54
BTO1-50 wt%	0.46	0.90
BTO2-33 wt%	0.40	1.45
BTO2-40 wt%	0.42	2.19
BTO2-set-33 wt%	0.40	1.53

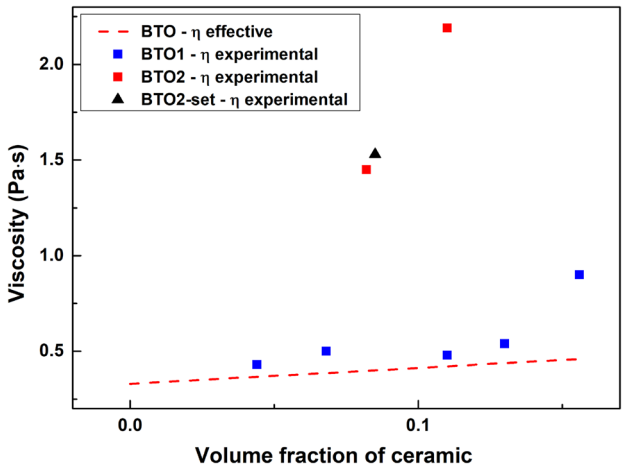

Fig. 9 Plot of the calculated and measured viscosities for BTO1 and BTO2 ceramic resins

the same order as the one experimentally measured. On the other hand, the BTO1-50 wt% resin (15.6 vol%) and all the BTO2 resins have a much higher viscosity (from 2 to 4 times higher) than the predicted effective viscosity, probably due to the larger ceramic loading (BTO1-50 wt%) and presence of nanosized particles (all BTO2 resins) causing interaction between the particles such that Eq. 3 is not valid [21].

3.6 Photocuring properties

Figure 10 shows the cure depth (C_d) as function of the applied energy dose for the base resin and the BTO1 and BTO2 resins, while Table 4 lists the curing properties extracted from these plots. In general, C_d decreases with increasing ceramic loading. There is a clear difference between the photocuring properties of the ceramic resins and the base resin, which is ascribed to light scattering due to the difference in refractive index between $BaTiO_3$ (2.4) [10, 22] and the photocurable resin (~1.5) [1] (see also Fig. 1). It is not expected that the $BaTiO_3$ powders absorb much light at the printing wavelength of 405 nm, as shown in Fig. 6.

For the BTO1 resins, the D_p decreases and the E_c has a decreasing trend with increasing ceramic loading. For ceramic resins that are controlled by scattering in addition to absorption, Eq. 2 can be rewritten to [1]:

$$C_d = \frac{2}{3}\frac{d\lambda}{\phi h \Delta n^2} ln\left(\frac{E}{E_c}\right), \quad (4)$$

where d is the mean particle size of the powder, λ is the wavelength of irradiation, ϕ is the volume fraction of the powder, h is the interparticle distance, and Δn is the difference in refractive index between the ceramic particles and the photocurable base resin. Thus, it is expected that the D_p decreases with increasing ceramic loading, due to scattering. The decreasing trend of E_c with increasing ceramic loading has also been predicted and observed by Tomeckova and Halloran [23] for SiO_2 and Al_2O_3 suspensions. Seemingly, an increase of the ceramic loading decreases the amount of energy required for initiating photopolymerization, E_c, by limiting photon penetration depth by scattering.

In contrast to the BTO1 resins, the BTO2 resins do not show a clear decreasing trend with increasing ceramic loading. While the BTO2-40 wt% resin had lower D_p and E_c than the BTO2-33 wt% resin, the BTO2-50 wt% resin had larger D_p and E_c compared to the BTO2-40 wt% resin. However, the viscosity of the BTO2-50 wt% was out of the range of the viscosimeter, so the resin may not be representative. BTO2 resins had a shorter cure depth than BTO1 resins (Table 4), in correlation with Eq. 4, as the mean particle size (d) is smaller for the milled BTO2 powder than for the milled BTO1 powder (Fig. 5b). The milled BTO2 powder also has a larger fraction of particles than BTO1 which are smaller than the wavelength, which is expected to increase the scattering. In addition, both the BTO1 and BTO2 resins have a large particle size distribution, which will decrease the C_d due to the presence of smaller particles [24].

The BTO2-set-33 wt% resin had a clearly larger C_d than the BTO2 resins (Table 4) due to the larger particles (agglomerates); however, the C_d was not larger than for the BTO1 resins, although the mean particle size was larger than for milled BTO1 (see Fig. 5b), which indicates that the nanosized particles in the larger BTO2-set agglomerates have an effect on the scattering, and not only the overall agglomerate size.

3.7 Printing of green parts

The BTO1 and BTO2 resins were used for printing green parts with various shapes (see Fig. 11). The applied settings for various printing trials are listed in Table 5. The

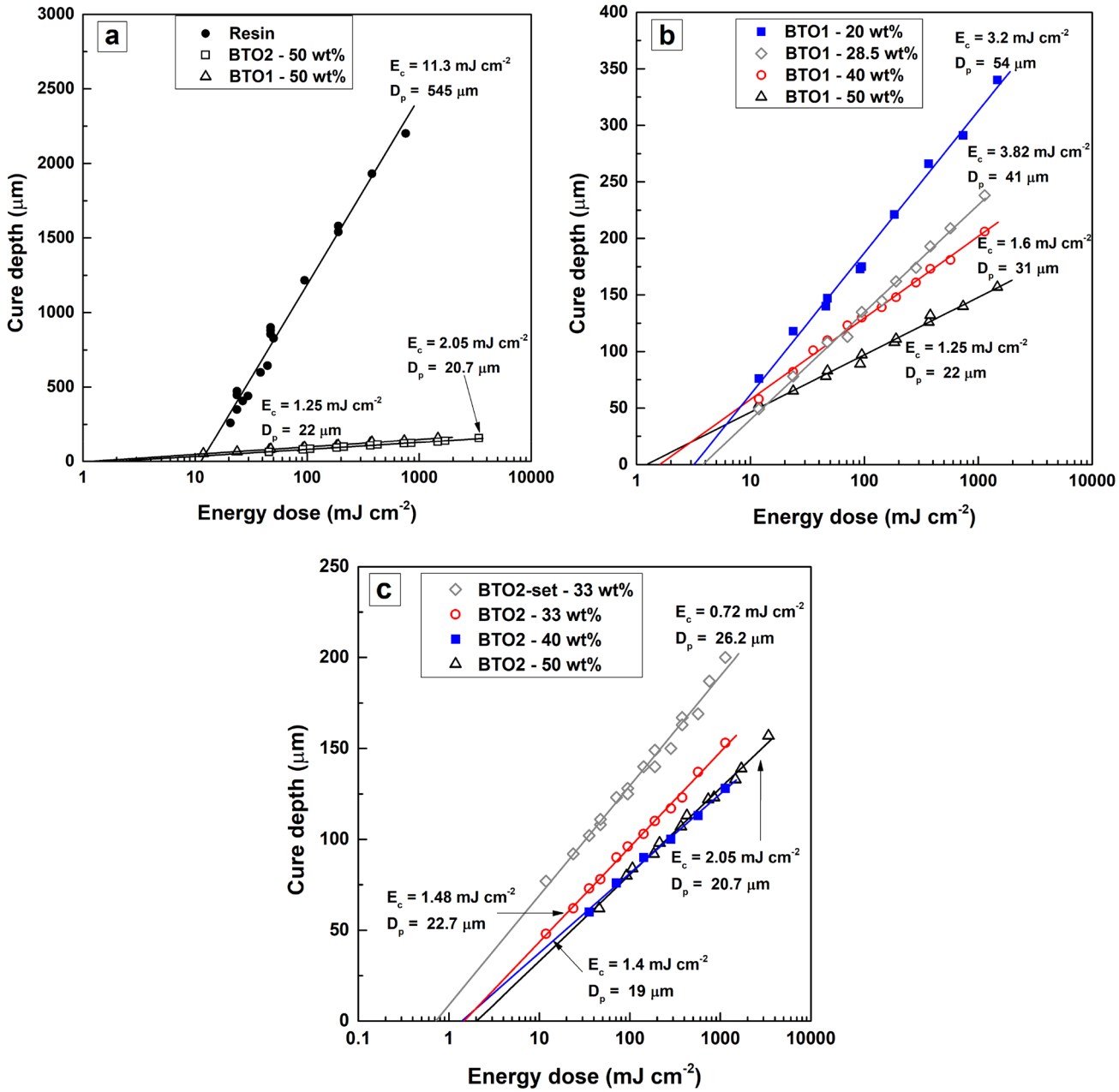

Fig. 10 Cure depth as a function of energy dose for: **a** base resin compared with 50 wt% BTO1 and BTO2 ceramic resins, **b** BTO1 ceramic resins, and **c** BTO2 and BTO2-set ceramic resins

overcuring was calculated as the percentage of cured thickness in excess of the set layer thickness, with respect to the experimentally determined C_d for the applied energy. By adjusting the layer thickness and the set energy to give a suitable overcuring (40–130%), all the ceramic resins could be successfully printed, except the BTO2-50 wt% resin, which had too high viscosity. For instance, the three cubes in Fig. 11a–c were printed with the same set layer thickness, but the set energy had to be increased for the BTO2-33 wt% resin compared to the two others to achieve sufficient overcuring, due to the smaller cure depth of that resin. If too high energy dose was applied, resulting in overcuring >200%, the printing typically failed as the print adhered to the bottom of the resin tank instead of to the printing platform.

An example of array shape printed with the BTO2-33 wt% ceramic resin (Fig. 11f, 93% overcuring) clearly shows scattering as the larger pillars on the right side have grown together. Scattering was observed for the printed objects as an extended cured, thin layer around the green

Table 4 Sensitivity (D_p), critical energy (E_c), and cure depth (C_d) at 100 mJ·cm^{-2}of ceramic resins, calculated based on the trendlines in Fig. 10

Resin	D_p (μm)	E_c (mJ·cm^{-2})	C_d at 100 mJ·cm^{-2} (μm)
Base resin (Genesis)	545	11.3	1188
BTO1-20 wt%	54	3.2	187
BTO1-28.5 wt%	41	3.8	135
BTO1-40 wt%	31	1.6	130
BTO1-50 wt%	22	1.2	97
BTO2-33 wt%	23	1.5	96
BTO2-40 wt%	19	1.4	81
BTO2-50 wt%	21	2.1	81
BTO2-set-33 wt%	26	0.7	129

parts. When decreasing the set energy (and thus the overcuring), scattering was less pronounced and better printing resolution was achieved. In general, the scattering effect increased with increased energy dose or increased ceramic loading. BTO1 ceramic resins showed less scattering than BTO2 ceramic resins as expected from the larger particle size of the BTO1 powder. For high accuracy printing with the nano-sized BTO2 resins, it will be important to reduce the layer thickness compared to the BTO1 resins to reduce the cure width caused by scattering, which will increase the printing time.

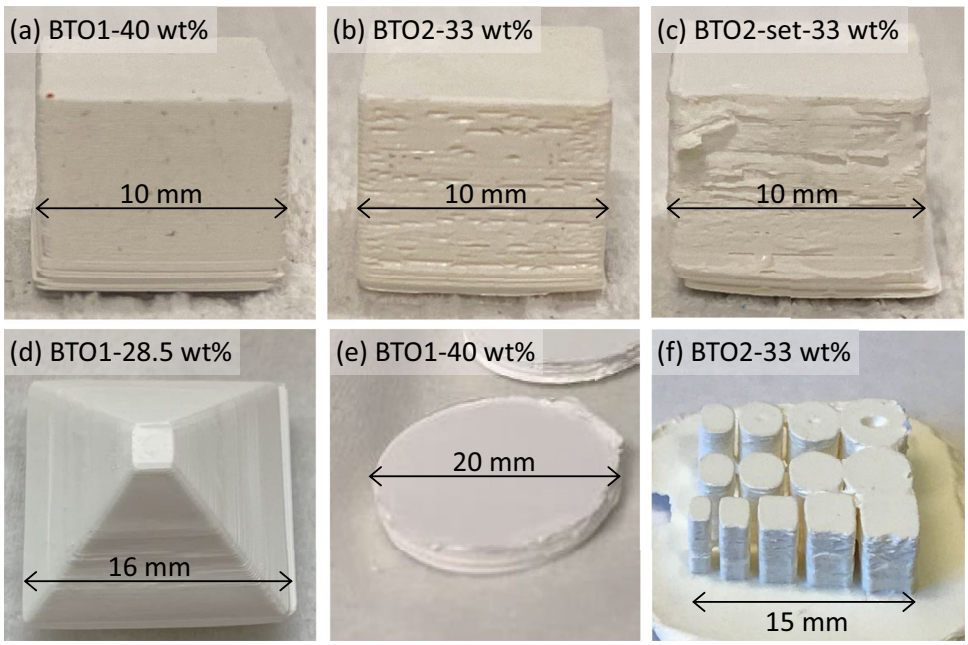

Fig. 11 Examples of printed green parts using different ceramic resins: **a**–**c** cubes, **d** pyramid, **e** pellet, and **f** array of tubes, cylinders, and square pillars with varying size

Table 5 Applied printing parameters for successfully printed green parts using different ceramic resins

Resin	Set layer thickness (μm)	Set energy (mW)	Calculated energy dose (mJ·cm^{-2})	Estimated C_d (μm)	Estimated overcuring (%)	Example of green part in Fig. 11
BTO1-20 wt%	50	32	23.7	108	116	–
BTO1-28.5 wt%	50	32	23.7	75	50	(d) Pyramid
	50	28	20.7	70	40	–
BTO1-40 wt%	50	32	23.7	84	68	(a) Cube (e) Pellet
BTO1-50 wt%	40	32	23.7	67	68	–
BTO2-33 wt%	40	62	45.9	77	93	(f) Array
	50	48	35.5	72	44	(b) Cube
BTO2-set-33 wt%	50	32	23.7	92	84	(c) Cube
	40	32	23.7	92	130	–

Cure depth and overcuring are estimated from the cure depth versus applied energy dose plots in Fig. 10

3.8 Outlook

Our results show that by using a commercial base resin without further development and a relatively simple stereolithography desktop 3D printer, it was possible to print with $BaTiO_3$ ceramic resins. However, it becomes challenging to print resins with higher ceramic loadings which is necessary to achieve ceramic parts with high final densities after thermal treatment (binder burnout and sintering). Thus, the use of this resin/printer system is probably limited to 3D printing of polymer/ceramic composites that can be used for instance as dielectric capacitors [25], or to 3D printing of highly porous ceramic scaffolds with high shrinkage rate which has been used to create complex ceramic scaffolds with higher resolution than the SLA printing resolution itself [26]. However, further development of the base resin and optimization of the ceramic powders are expected to facilitate an increased ceramic loading of printable ceramic resins. For instance, instead of using the standard Tethon 3D Genesis development resin, the use of the same supplier's "High load" or "Flexible" Genesis development resins [27] should allow a larger fraction of ceramic powder to be included, but these were not available when this work started. Another option is to decrease the refractive index difference between the base resin and ceramic powder by modifying the resin with heavier elements such as sulfur to increase the refractive index of the base resin [28].

Optimization of the morphology and particle size distribution of the ceramic powder can increase the ceramic loading in the resin. Farris [29] and Bae [12] calculated the relative viscosities of bi-modal powder systems versus blend ratio, showing that changing the particle size distribution from monomodal to bimodal mixture of coarse and fine particles can decrease the relative viscosity with more than one order of magnitude. The fraction of solids can be increased from 60 to 75 vol%, without changing the viscosity of the original suspension. While small particles are desired for optimal sintering driving force, larger particles decrease the light scattering during the photopolymerization reaction. Thus, a possible solution to improve the curing properties is granulation of nano-powders or submicron powders to microspheres, which has been used in fabrication of high dielectric constant polymer-matrix composites with $BaTiO_3$ [21], as the microspheres increase the fluidity and maintain low viscosity of the ceramic suspensions.

The desktop 3D printer used in our work relies on self-levelling of the resin for recoating of each layer and this approach makes it challenging to use a highly viscous ceramic resin. In contrast, advanced 3D printers for ceramics typically use a doctor blade or another recoating method to ensure renewal of the viscous ceramic resin for each layer to be cured, a procedure similar to slurry tape casting process, but such printers are much more expensive than desktop 3D printers. For instance, Chen et al. [30] and Song et al. [15] reported successful printing of $BaTiO_3$ ceramic resins with ceramic loading of 70 wt% using an advanced printer with a doctor blade for recoating.

4 Conclusions

The properties of two $BaTiO_3$ powders and their respective ceramic resins have been characterized and evaluated for stereolithography 3D printing using a desktop 3D printer. The two powders had different particle size distribution: the micro-sized powder (BTO1) with grains in the range 1-20 µm had a narrower particle size distribution with larger and more compact agglomerates, while the nano-sized powder (BTO2) with grains in the range 60–100 nm had a broader particle size distribution with 3 fractions of agglomerates which were more porous. The BTO1 and BTO2 powder adsorbed at 381 nm and 366 nm, respectively, which is lower than the printing wavelength (405 nm), thus absorption of light does not hinder the curing of the resins. Compared to the BTO2 resins, the BTO1 resins had a lower viscosity and a larger cure depth due to the larger particle size which reduces the scattering of light and is beneficial for printing. Both powders could be used to 3D print green parts by adjusting the printing parameters to account for the different cure depths. To achieve similar lateral printing resolution with the BTO2 resins as with the BTO1 resins, the lower cure depth of the BTO2 resins will require a smaller layer thickness to reduce the cure width due to the larger scattering in the BTO2 resins with smaller particles.

Acknowledgements Ruth Elisabeth Stensrød is acknowledged for performing the XRD measurements, Mathieu Grandcolas is acknowledged for performing the UV–Vis absorption measurements, and Martin Fleissner Sunding is acknowledged for acquiring the SEM images. This work was financially supported by the Research Council of Norway through the basic grant to SINTEF received by the internal project "3D printing of piezoelectric transducer array".

Author contributions HR and PMR initiated and led the work. ES, TD, and TOS designed the experiments, with contribution from MLF, HR, and PMR. All authors contributed to the analysis or interpretation of data. ES did most of the experimental work, with assistance from TD on the 3D printing. ES, MLF, and PMR wrote the manuscript and TD, TOS, and HR approved it.

Funding Open access funding provided by SINTEF.

Data availability The data that support the findings of this study are available from the corresponding author upon reasonable request.

Declarations

Conflict of interest The authors have no competing interests to declare that are relevant to the content of this article.

References

1. Zakeri S, Vippola M, Levänen E (2020) A comprehensive review of the photopolymerization of ceramic resins used in stereolithography. Addit Manuf 35:101177. https://doi.org/10.1016/j.addma.2020.101177
2. Chen Z, Li Z, Li J et al (2019) 3D printing of ceramics: a review. J Eur Ceram Soc 39:661–687. https://doi.org/10.1016/j.jeurceramsoc.2018.11.013
3. Halloran J (2016) Ceramic Stereolithography: additive manufacturing for ceramics by photopolymerization. Annu Rev Mater Res 46:19–40. https://doi.org/10.1146/annurev-matsci-070115-031841
4. Bae C-J, Ramachandran A, Chung K et al (2017) Ceramic stereolithography: additive manufacturing for 3D complex ceramic structures. J Korean Ceram Soc 54:470–477. https://doi.org/10.4191/kcers.2017.54.6.12
5. Komissarenko DA, Sokolov PS, Evstigneeva AD et al (2018) Rheological and curing behavior of acrylate-based suspensions for the DLP 3D printing of complex zirconia parts. Materials (Basel) 11:2350. https://doi.org/10.3390/ma11122350
6. Westbeek S, van Dommelen JAW, Remmers JJC, Geers MGD (2018) Multiphysical modeling of the photopolymerization process for additive manufacturing of ceramics. Eur J Mech A Solids 71:210–223. https://doi.org/10.1016/j.euromechsol.2018.03.020
7. Gentry SP, Halloran JW (2013) Depth and width of cured lines in photopolymerizable ceramic suspensions. J Eur Ceram Soc 33:1981–1988. https://doi.org/10.1016/j.jeurceramsoc.2013.02.033
8. Gentry SP, Halloran JW (2015) Light scattering in absorbing ceramic suspensions: effect on the width and depth of photopolymerized features. J Eur Ceram Soc 35:1895–1904. https://doi.org/10.1016/j.jeurceramsoc.2014.12.006
9. Hervé P, Vandamme LKJ (1994) General relation between refractive index and energy gap in semiconductors. Infrared Phys Technol 35:609–615. https://doi.org/10.1016/1350-4495(94)90026-4
10. Lamichhane A, Ravindra NM (2020) Energy gap-refractive index relations in Perovskites. Materials (Basel) 13:1917. https://doi.org/10.3390/ma13081917
11. Wang W, Sun J, Guo B et al (2020) Fabrication of piezoelectric nano-ceramics via stereolithography of low viscous and non-aqueous suspensions. J Eur Ceram Soc 40:682–688. https://doi.org/10.1016/j.jeurceramsoc.2019.10.033
12. Bae C-J (2008) Integrally cored ceramic investment casting mold fabricated by ceramic stereolithography. Dissertation, University of Michigan
13. Cheng N-S, Law AW-K (2003) Exponential formula for computing effective viscosity. Powder Technol 129:156–160. https://doi.org/10.1016/S0032-5910(02)00274-7
14. Einstein A (1906) Eine neue Bestimmung der Moleküldimensionen. Ann Phys 324:289–306. https://doi.org/10.1002/andp.19063240204
15. Song X, Chen Z, Lei L et al (2017) Piezoelectric component fabrication using projection-based stereolithography of barium titanate ceramic suspensions. Rapid Prototyp J 23:44–53. https://doi.org/10.1108/RPJ-11-2015-0162
16. Buscaglia V, Randall CA (2020) Size and scaling effects in barium titanate. An overview J Eur Ceram Soc 40:3744–3758. https://doi.org/10.1016/j.jeurceramsoc.2020.01.021
17. Suzuki K, Kijima K (2005) Optical band gap of barium titanate nanoparticles prepared by RF-plasma chemical vapor deposition. Jpn J Appl Phys 44:2081. https://doi.org/10.1143/JJAP.44.2081
18. Murray CB, Norris DJ, Bawendi MG (1993) Synthesis and characterization of nearly monodisperse CdE (E = sulfur, selenium, tellurium) semiconductor nanocrystallites. J Am Chem Soc 115:8706–8715. https://doi.org/10.1021/ja00072a025
19. Smirnov A, Chugunov S, Kholodkova A et al (2021) Progress and challenges of 3D-printing technologies in the manufacturing of piezoceramics. Ceram Int 47:10478–10511. https://doi.org/10.1016/j.ceramint.2020.12.243
20. Smirnov A, Chugunov S, Kholodkova A et al (2022) The fabrication and characterization of $BaTiO_3$ piezoceramics using SLA 3D printing at 465 nm wavelength. Materials (Basel) 15:960. https://doi.org/10.3390/ma15030960
21. Li W-D, Wang C, Jiang Z-H et al (2020) Stereolithography based additive manufacturing of high-k polymer matrix composites facilitated by thermal plasma processed barium titanate microspheres. Mater Des 192:108733. https://doi.org/10.1016/j.matdes.2020.108733
22. Nomoto H, Mori Y, Matsuo H (2014) Barium titanate dispersion obtained by a high pressure methods and light resistant composites containing the nanoparticles. J Ceram Soc Jpn 122:129–133. https://doi.org/10.2109/jcersj2.122.129
23. Tomeckova V, Halloran JW (2010) Critical energy for photopolymerization of ceramic suspensions in acrylate monomers. J Eur Ceram Soc 30:3273–3282. https://doi.org/10.1016/j.jeurceramsoc.2010.08.003
24. Sun C, Zhang X (2002) The influences of the material properties on ceramic micro-stereolithography. Sens Actuator A Phys 101:364–370. https://doi.org/10.1016/S0924-4247(02)00264-9
25. Yang Y, Chen Z, Song X et al (2016) Three dimensional printing of high dielectric capacitor using projection based stereolithography method. Nano Energy 22:414–421. https://doi.org/10.1016/j.nanoen.2016.02.045
26. Gao Y, Ding J (2020) Low solid loading, low viscosity, high uniform shrinkage ceramic resin for stereolithography based additive manufacturing. Procedia Manuf 48:749–754. https://doi.org/10.1016/j.promfg.2020.05.109
27. Tethon 3D, https://tethon3d.com/, Accessed 17 Mar 2022
28. Kim H, Yeo H, Goh M et al (2016) Preparation of UV-curable acryl resin for high refractive index based on 1,5-bis(2-acryloylenethyl)-3,4-ethylenedithiothiophene. Eur Polym J 75:303–309. https://doi.org/10.1016/j.eurpolymj.2015.12.016
29. Farris RJ (1968) Prediction of the viscosity of multimodal suspensions from unimodal viscosity data. Transact Soc Rheol 12:281–301. https://doi.org/10.1122/1.549109
30. Chen Z, Song X, Lei L et al (2016) 3D printing of piezoelectric element for energy focusing and ultrasonic sensing. Nano Energy 27:78–86. https://doi.org/10.1016/j.nanoen.2016.06.048